



Aalborg Universitet

AALBORG UNIVERSITY
DENMARK

Design of PWM-SMC Controller Using Linearized Model for Grid-Connected Inverter With LCL Filter

Li, Han ; Wu, Weimin; Huang, Min; Chung, Henry; Liserre, Marco; Blaabjerg, Frede

Published in:
I E E E Transactions on Power Electronics

DOI (link to publication from Publisher):
[10.1109/TPEL.2020.2990496](https://doi.org/10.1109/TPEL.2020.2990496)

Publication date:
2020

Document Version
Accepted author manuscript, peer reviewed version

[Link to publication from Aalborg University](#)

Citation for published version (APA):
Li, H., Wu, W., Huang, M., Chung, H., Liserre, M., & Blaabjerg, F. (2020). Design of PWM-SMC Controller Using Linearized Model for Grid-Connected Inverter With LCL Filter. *I E E E Transactions on Power Electronics*, 35(12), 12773-12786. [9079202]. <https://doi.org/10.1109/TPEL.2020.2990496>

General rights

Copyright and moral rights for the publications made accessible in the public portal are retained by the authors and/or other copyright owners and it is a condition of accessing publications that users recognise and abide by the legal requirements associated with these rights.

- Users may download and print one copy of any publication from the public portal for the purpose of private study or research.
- You may not further distribute the material or use it for any profit-making activity or commercial gain
- You may freely distribute the URL identifying the publication in the public portal -

Take down policy

If you believe that this document breaches copyright please contact us at vbn@aub.aau.dk providing details, and we will remove access to the work immediately and investigate your claim.

Design of PWM-SMC Controller Using Linearized Model for Grid-Connected Inverter with LCL Filter

Han Li, Weimin Wu, *Member, IEEE*, Min Huang, Henry Shu-hung Chung, *Fellow, IEEE*, Marco Liserre, *Fellow, IEEE*, and Frede Blaabjerg, *Fellow, IEEE*

Abstract— Nowadays, various Sliding Mode Control (SMC) methods have been successfully applied to digitally controlled Grid-Connected Inverter (GCI) with LCL filter. However, how to design of the Pulse Width Modulation based SMC (PWM-SMC) controller need to be further explored, especially upon the large variation of parameters drift and the delay issue. In this paper, the essence of two classic SMC methods used in power converter area is first analyzed in detail. Thus, a novel design of PWM-SMC controller using linearized model for three-phase GCI with LCL filter is proposed. Based on this, a three-loop step-by-step design of the PWM-SMC controller is developed, by using the closed-loop pole locations. Robust analysis against parameters drift is also studied. In addition, a discrete state observer is adopted to reduce the number of sensors. Further, a discussion between the proposed control strategy with the existing SMC methods and the full-state feedback controller is carried out. Finally, a 3 kW lab device designed on the dSPACE is constructed to verify the feasibility of the proposed strategy and the correctness of theoretical analysis¹.

Index Terms— Grid-connected inverter, LCL-filter, Parameters drift, Robust, Sliding Mode Control, Stability analysis, State Observer.

I. INTRODUCTION

Due to the environmental concerns and fossil energy crisis problems, in recent years, researches on the renewable energy grid-connected power generation technology have received extensive attention [1]. As the core component of system, the Grid-Connected Inverter (GCI) is charged with the task of injecting high-quality current into power grid in a stable and efficient way. For this purpose, a power filter (L or LCL) is often used to suppress the high-frequency

harmonics generated by switching operations. Compared with the L filter, a third-order LCL filter has been widely adopted, owing to its better ability to attenuate high-frequency harmonics with relatively smaller inductance [2]. However, it has inherent resonant problem that may seriously deteriorate the stability of whole system [3]–[5], especially when grid distortion and parameters drift occur in GCI systems, resulting in a critical challenge in the current regulator design.

Nowadays, to improve the stability, many linear controllers combined with active damping methods have been applied to LCL -filtered GCI [6]–[12]. Besides, various nonlinear controllers have been deeply studied, such as predictive controller [13]–[16], Lyapunov-Function based controller [17], passive based controller [18]–[20], adaptive controller [21], [22], deadbeat controller [23]–[25] and SMC controller [26]–[31], etc. As one of nonlinear controllers, the SMC controller has attracted many interests, due to its strong robustness against system parameter uncertainties.

Currently, according to the switching mode, there are two kinds of SMC controllers for LCL -filtered GCI. The one is the hysteresis modulation based SMC (HM-SMC) [26]–[27], while the other is the Pulse Width Modulation based SMC (PWM-SMC) [29]–[31].

In HM-SMC methods, Komurcugil *et al.* [26] had proposed a new sliding surface function with double-band hysteresis scheme, which can reduce the number of the sensors and achieve good dynamic performance. Guzman *et al.* [27] had integrated kalman filter (KF) with SMC controller for LCL -filtered inverters, using a reduced model to achieve high robustness against LCL parameters drift. Also, Guzman *et al.* [28] had proposed a control algorithm in natural frame based on SMC together with KF to obtain three decoupled controllers, which can provide the desired dynamics for the grid-injected current. However, the hysteresis modulation will cause the variable switching frequency, resulting in the difficulty of designing the output power filter. Besides, a high sampling frequency has to be adopted for the HM-SMC, increasing the implementation difficulty.

The PWM-SMC can realize the fixed switching frequency operation. Hao *et al.* [29] adopted the equivalent SMC and inserted the multiple resonant terms into the sliding surface function, which can eliminate steady-state error and suppress the total harmonic distortion (THD) of the grid current effectively. Vieira *et al.* [30] introduced a dual-loop design strategy and chose the discrete-time SMC controller as the inner loop controller to simplify the current control design. Alali *et al.* [31] studied two continuous SMC algorithms to prevent very high-frequency switching effects of the SMC. Although all the mentioned PWM-SMC methods can achieve good control performance, the detailed

Manuscript received August 28, 2019; revised November 12, 2019; revised January 11, 2020; accepted March 11, 2020. Date of publication; date of current version. This work was supported in part by the National Natural Science Foundation of China under Grant 51877130, in part by the National Natural Science Foundation of China under Grant 51561165013, in part by the Shanghai Science and Technology Commission under Grant 17040501500, and in part by the National Key Research and Development Project of China under Grant 2017YFGH001164.

Recommended for publication by Associate Editor *****.
(Corresponding author: Weimin Wu.)

H. Li, W. Wu and M. Huang are with the Electrical Engineering Department, Shanghai Maritime University, Shanghai 201306, China (e-mail: 626142955@qq.com; wmmu@shmtu.edu.cn; minhuang@shmtu.edu.cn).

H. S.-H. Chung is with the Department of Electrical Engineering and the Centre for Smart Energy Conversion and Utilization Research, City University of Hong Kong, Hong Kong (e-mail: eeshc@cityu.edu.hk).

M. Liserre is with the Chair of Power Electronics, Christian-Albrechts University of Kiel, Kiel 24143, Germany (e-mail: ml@tf.uni-kiel.de).

F. Blaabjerg is with the Energy Engineering Department, Aalborg University, Aalborg 9100, Denmark (e-mail: fbj@et.aau.dk).

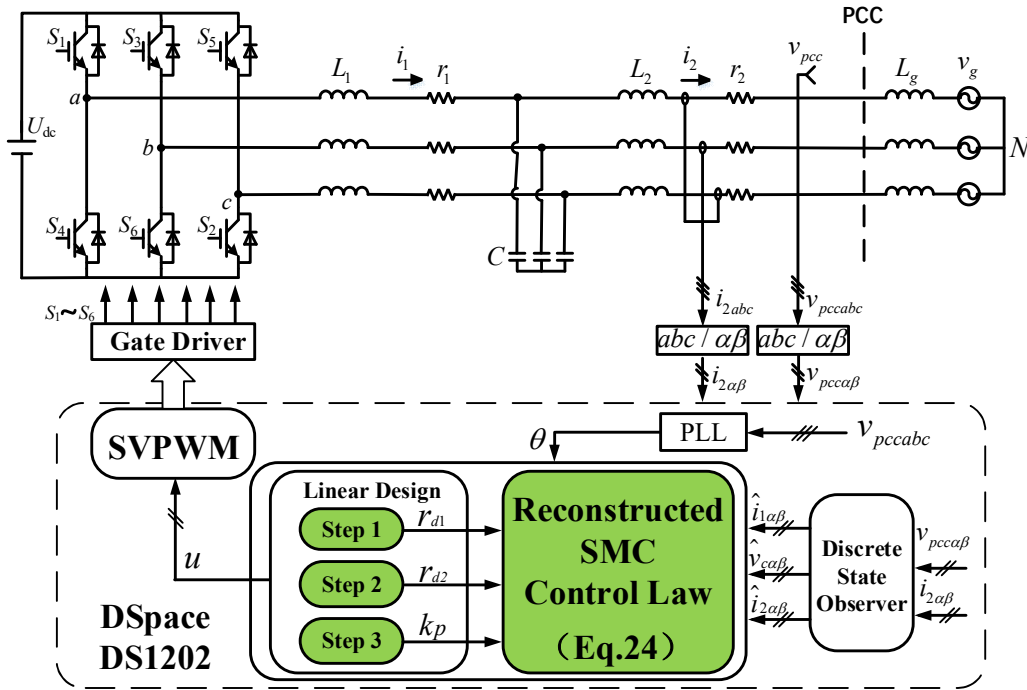


Fig. 1. Three-phase LCL -filtered GCI with the proposed design of SMC controller using linearized model.

design guideline of controller parameters is lacking, resulting in the industrial application difficulty.

Aiming at the industrial application, different from the traditional PWM-SMC design based on Lyapunov stability, this paper proposes a step-by-step design guideline of PWM-SMC controller using linearized model for three-phase LCL -filtered GCIs, which can help engineers to precisely design a highly robust PWM-SMC controller to against the output filter parameters drift.

The rest of this paper is organized as follows: Section II first presents the accurate error dynamics modeling of GCI with LCL filter. Then, the essence of HM-SMC and PWM-SMC is explored in detail in Section III. Based on the above, Section IV proposes a novel design of SMC controller using linearized model together with a step-by-step parameter tuning and robustness analysis. Further, Section V briefly introduces how to adopt a discrete state observer to save sensors, while Section VI demonstrates the experimental validation results on a 3 kW/3-phase/110 V experimental lab setup. Section VII discusses the comparison between the proposed control strategy with the existing SMC methods and the full-state feedback controller. Finally, Section VIII draws some conclusions.

II. ERROR DYNAMICS MODELING OF GCI WITH LCL FILTER

Fig. 1 shows the three-phase LCL -filtered GCI and its basic control structure, where the LCL filter consists of an inverter-side inductor of L_1 , a capacitor of C , and a grid-side inductor of L_2 . The equivalent grid impedance is modeled with the inductor of L_g . The Point of Common Coupling (PCC) voltage $v_{pcc} = [v_{pcca} \ v_{pccb} \ v_{pccc}]^T$, the inverter-side current $i_1 = [i_{1a} \ i_{1b} \ i_{1c}]^T$, the capacitor voltage $v_c = [v_{ca} \ v_{cb} \ v_{cc}]^T$, and the grid-injected current

$i_2 = [i_{2a} \ i_{2b} \ i_{2c}]^T$ are sensed or calculated for the controller.

The operation of system in $\alpha\beta$ reference frame can be described by the following equations:

$$L_1 \frac{di_{1\alpha}}{dt} = u_{1\alpha} - i_{1\alpha}r_1 - v_{c\alpha} \quad (1),$$

$$L_1 \frac{di_{1\beta}}{dt} = u_{1\beta} - i_{1\beta}r_1 - v_{c\beta} \quad (2),$$

$$C \frac{dv_{c\alpha}}{dt} = i_{1\alpha} - i_{2\alpha} \quad (3),$$

$$C \frac{dv_{c\beta}}{dt} = i_{1\beta} - i_{2\beta} \quad (4),$$

$$L_2 \frac{di_{2\alpha}}{dt} = v_{c\alpha} - i_{2\alpha}r_2 - v_{pcc\alpha} \quad (5),$$

$$L_2 \frac{di_{2\beta}}{dt} = v_{c\beta} - i_{2\beta}r_2 - v_{pcc\beta} \quad (6),$$

where $u_{ik(k=\alpha,\beta)}$ is the switching function, and r_1 , r_2 are the equivalent resistances of inductors L_1 and L_2 , respectively.

According to the angle generated by the Phase-Locked Loop (PLL) and the given reference current, the reference of grid-injected current i_2^* can be obtained. Furthermore, based on (1)-(6), the reference of the inverter-side current i_1^* and the reference of capacitor voltage v_c^* can be also derived. Then three references of the state variables are

$$\begin{cases} i_{2k}^* = I_2 \sin(\omega t + \theta) \\ v_{ck}^* = L_2 \dot{i}_{2k}^* + v_{pcc} + i_{2k}^* r_2 \\ i_{1k}^* = i_{2k}^* + C \dot{v}_{ck}^* \end{cases} \quad k = \alpha, \beta \quad (7).$$

Note that the α -axis and the β -axis are independent with each other. In order to facilitate the description, the next

design focuses on the α -axis, while the design in the β -axis is the same as the one in the α -axis.

Define three system error dynamics as,

$$\begin{cases} x_{e1} = i_1^* - i_1 \\ x_{e2} = v_c^* - v_c \\ x_{e3} = i_2^* - i_2 \end{cases} \quad (8),$$

where their derivatives are

$$\begin{aligned} \dot{x}_{e1} &= \dot{i}_1^* - \dot{i}_1 = \dot{i}_1^* - \left(\frac{1}{L_1} (u_i - i_1 r_1 + i_1^* r_1 - i_1^* r - v_c + v_c^* - v_c^*) \right) \\ &= -\frac{1}{L_1} x_{e2} - \frac{r_1}{L_1} x_{e1} - \frac{1}{L_1} u_i + \dot{i}_1^* + \frac{v_c^*}{L_1} + \frac{r_1}{L_1} i_1^* \end{aligned} \quad (9),$$

$$\dot{x}_{e2} = \dot{v}_c^* - \dot{v}_c = \frac{1}{C} (i_1^* - i_2^*) - \frac{1}{C} (i_1 - i_2) = \frac{1}{C} x_{e1} - \frac{1}{C} x_{e3} \quad (10),$$

$$\begin{aligned} \dot{x}_{e3} &= \dot{i}_2^* - \dot{i}_2 = \frac{1}{L_2} (v_c^* - i_2^* r_2 - v_{pcc}) - \frac{1}{L_2} (v_c - i_2 r_2 - v_{pcc}) \\ &= \frac{1}{L_2} x_{e2} - \frac{r_2}{L_2} x_{e3} \end{aligned} \quad (11).$$

The state-space expression of system error dynamics can be achieved as

$$\begin{aligned} \dot{x}_e &= Ax_e + Bu_i + D \\ \begin{bmatrix} \dot{x}_{e1} \\ \dot{x}_{e2} \\ \dot{x}_{e3} \end{bmatrix} &= \begin{bmatrix} -\frac{r_1}{L_1} & -\frac{1}{L_1} & 0 \\ \frac{1}{C} & 0 & -\frac{1}{C} \\ 0 & \frac{1}{L_2} & -\frac{r_2}{L_2} \end{bmatrix} \begin{bmatrix} x_{e1} \\ x_{e2} \\ x_{e3} \end{bmatrix} + \begin{bmatrix} -\frac{1}{L_1} \\ 0 \\ 0 \end{bmatrix} \begin{bmatrix} u_i \\ 0 \\ 0 \end{bmatrix} + \begin{bmatrix} d_e \\ 0 \\ 0 \end{bmatrix} \end{aligned} \quad (12),$$

$$\text{where } d_e = \dot{i}_1^* + \frac{v_c^*}{L_1} + \frac{r_1 i_1^*}{L_1}.$$

III. ESSENCE OF HM-SMC AND PWM-SMC

A. Basic Principle of SMC Theory

For a given control system represented by the state equation

$$\dot{x} = A(x, t) + B(x, t)u \quad (13).$$

In order to construct a SMC system, the following two steps are needed [32]:

- 1) Design a sliding surface $S(x) = 0$ to represent a desired system dynamics.
- 2) Design a variable structure control $u(x, t)$ as

$$u(x, t) = \begin{cases} u^+(x, t) & \text{when } S(x) > 0 \\ u^-(x, t) & \text{when } S(x) < 0 \end{cases} \quad (14).$$

Any state x outside the sliding surface can be driven to reach the sliding surface in finite time. On the sliding surface, the sliding mode takes place, following the desired system dynamics.

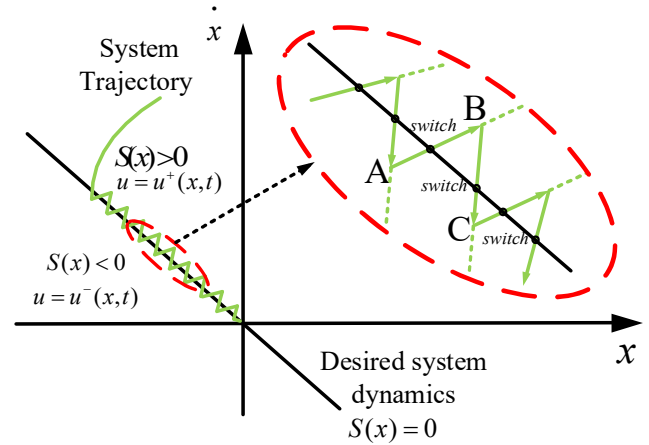


Fig. 2. Basic Principle of Practical SMC System.

Fig. 2 introduces the basic principle of practical SMC system. The middle black line represents the sliding surface $S(x) = 0$, which is the desired system dynamics. The sliding surface divides the system state into two different parts, where different control $u(x, t)$ works. Under this variable structure control, the green solid line depicts the system trajectory.

As shown in Fig. 2, when the system state is at point A, the sliding surface function $S(x)$ is less than zero, and then $u^-(x, t)$ controls the system state to move towards the sliding surface. When the system state reaches the sliding surface, it crosses the sliding surface under the control of $u^-(x, t)$. At this time, the system switches to the control of $u^+(x, t)$ immediately. Due to the inertia (space or time lag), the system state can only gradually stop at point B. Then the system state moves from point B towards point C, according to the previous motion mode. The dashed line represents that the trajectory of system state would be unstable without the switching control.

Through the above analysis, we can find that switching plays an important role in SMC system. For example, the reaching law approach is an effective way to design the SMC system [33], which directly specifies the dynamics of the sliding surface function,

$$\dot{S} = -kS - \varepsilon \text{sgn}(S) \quad (15).$$

The symbolic function could enable the system state to have a certain rate when reaching the sliding surface, so that the system state can cross the sliding surface. Therefore, in a conventional SMC system, the switching of system can be realized by the symbolic function in (15). However, in practical applications, the switching modes are various, especially for power-electronic-based systems with two special modulation modes. Here, a single-phase full-bridge GCI with an L filter is taken as an example to simply elaborate the switching characteristic in HM-SMC and PWM-SMC in following two subsections.

B. Switching Characteristic in HM-SMC

Fig. 3 shows the operation of HM-SMC, where this method adopts the hysteresis modulation to achieve a high frequency switching action. For conveniently describing the system, the sliding surface function is chosen as the error of

the inverter side current of $(i_1^* - i_1)$.

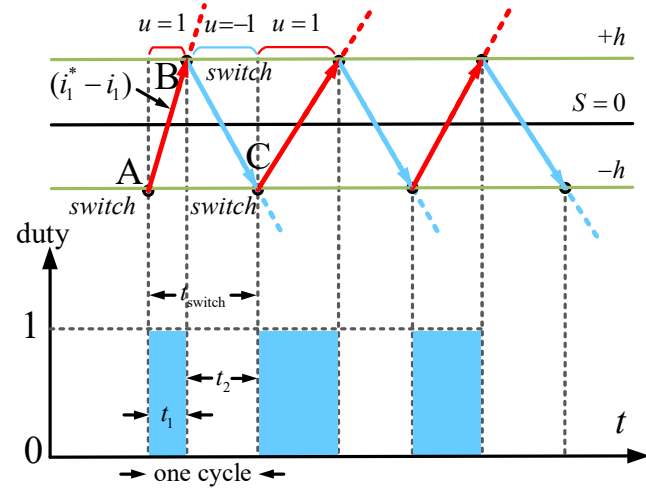


Fig. 3. Operation of HM-SMC.

The switching action can be written as

$$u = \begin{cases} -1 & S \geq +h \\ 1 & S \leq -h \end{cases} \quad (16),$$

where in the other case $(-h < S < +h)$, the switching action keep the former state. h is the width of the hysteresis band, which controls the switching frequency.

As shown in Fig. 3, the hysteresis modulator employs a hysteresis band with the boundary layer to switch the control of the system. In one switching cycle, there are two periods t_1 and t_2 , where the switching actions are $u = 1$ and $u = -1$ respectively.

When the sliding surface function $S(x)$ is equal to the value of the lower boundary layer $(-h)$ at point A, the switching occurs and the switching action is $u = 1$. During the switching action of $u = 1$, the sliding surface function $S(x)$ moves from $-h$ toward $+h$.

When the sliding surface function $S(x)$ is equal to the value of the upper the boundary layer $(+h)$ at point B, the switching occurs and the switching action is $u = -1$. During the switching action of $u = -1$, the sliding surface function $S(x)$ moves from $+h$ toward $-h$.

Stated thus, the hysteresis modulator ensures the switching of the HM-SMC system.

C. Switching Characteristic in PWM-SMC

As shown in Fig. 4, different from the HM-SMC, the PWM-SMC adopts pulse width modulator to control the system state to move towards the sliding surface indirectly. In one switching cycle, there are two circuit states, where the switching actions are $u = -1$ and $u = 1$ respectively.

When the system state is at point A, modulation wave u_i intersects the carrier, the switching occurs and the switching action is $u = 1$. During the switching action of $u = 1$, the sliding surface function $S(x)$ moves from negative toward positive.

When the system state is at point B, modulation wave u_i intersects the carrier again, the switching occurs and the switching action is $u = -1$. During the switching action of $u = -1$, the sliding surface function $S(x)$ moves from positive toward negative.

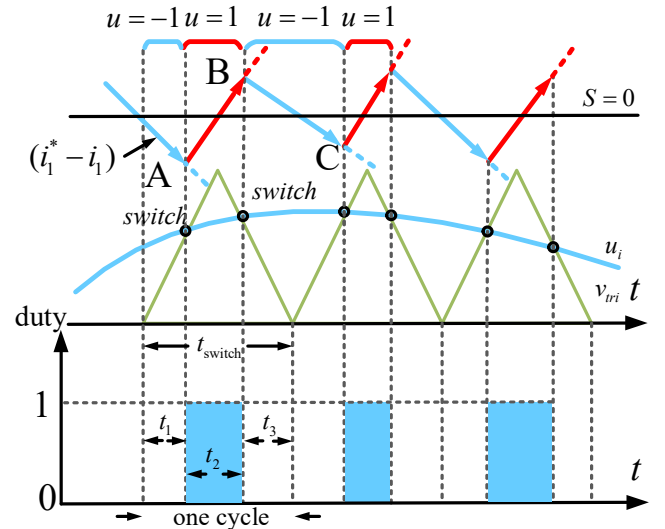


Fig. 4. Operation of PWM-SMC.

Similar to HM-SMC, pulse width modulator can also ensure the switching of the PWM-SMC system. Although the conclusion is based on a single-phase GCI system, it can be extended to a three-phase GCI system.

Therefore, different from the conventional PWM-SMC design with the nonlinear term in u_i , the nonlinear term will be eliminated in the proposed design process, where the linear tool can be utilized to analyze the stability. Note that during the design, PWM-SMC systems in [34]-[36] had also ignored the nonlinear term in the control law.

IV. PROPOSED DESIGN OF PWM-SMC CONTROLLER USING LINEARIZED MODEL

A. Proposed Reconstructed Control Law with Zero Steady-State Error

The LCL-filtered GCI is a typical third-order system. In order to guarantee the global stability and damping effect, we choose the sum of three error dynamics as the sliding surface function, which is defined as [29]

$$\begin{aligned} S &= C_e x_e \\ &= \alpha_1 x_{e1} + \alpha_2 x_{e2} + \alpha_3 x_{e3} \\ &= \alpha_1 (i_1^* - i_1) + \alpha_2 (v_c^* - v_c) + \alpha_3 (i_2^* - i_2) \end{aligned} \quad (17).$$

Through the above analysis, the switching function can be realized by PWM, thus the symbolic function is eliminated, the reaching law is rewritten as

$$\dot{S} = -kS \quad (18),$$

Based on (17)-(18), a control law is deduced as

$$\begin{aligned} u_i &= -r_1 x_1 - x_2 + L_1 \dot{i}_1^* + v_c^* + r_1 i_1^* + L_1 \frac{\alpha_2}{\alpha_1} \left(\frac{1}{C} x_1 - \frac{1}{C} x_3 \right) \\ &\quad + L_1 \frac{\alpha_3}{\alpha_1} \left(\frac{1}{L_2} x_2 - \frac{r_2}{L_2} x_3 \right) + k \frac{L_1}{\alpha_1} S \end{aligned} \quad (19).$$

Through (19), we find that the control law is complex, resulting in the difficulty to design controller parameters.

Separating the sliding surface function, the control law can be rewritten as,

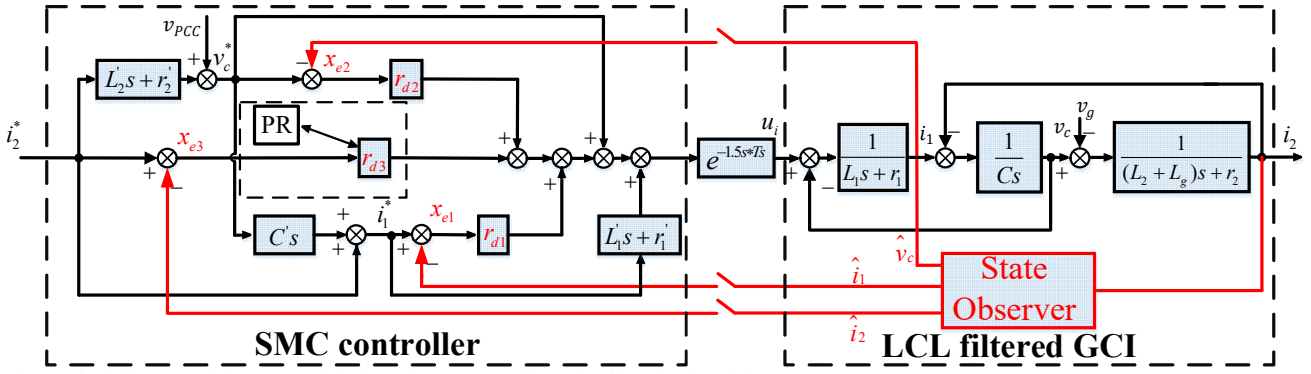


Fig. 5. Block diagram of the proposed design of SMC controller using linearized model.

$$\begin{aligned} u_i = & L_1 \dot{i}_1^* + v_c^* + r_1 \dot{i}_1^* + (-r_1 + L_1 \frac{\alpha_2}{\alpha_1} \frac{1}{C} + kL_1) x_{e1} \\ & + (-1 + L_1 \frac{\alpha_3}{\alpha_1} \frac{1}{L_2} + k \frac{L_1}{\alpha_1} \alpha_2) x_{e2} \\ & + (-L_1 \frac{\alpha_2}{\alpha_1} \frac{1}{C} - L_1 \frac{\alpha_3}{\alpha_1} \frac{r_2}{L_2} + k \frac{L_1}{\alpha_1} \alpha_3) x_{e3} \end{aligned} \quad (20).$$

As shown in (20), the gain of each state feedback variable is determined by three or four sliding mode parameters (sliding surface function parameters and the gain of the reaching law). Based on (20), by simplifying the control law and reintegrating the sliding mode parameters, three new uncoupled controller parameters can be obtained. They are

$$r_{d1} = (-r_1 + L_1 \frac{\alpha_2}{\alpha_1} \frac{1}{C} + kL_1) \quad (21)$$

$$r_{d2} = (-1 + L_1 \frac{\alpha_3}{\alpha_1} \frac{1}{L_2} + k \frac{L_1}{\alpha_1} \alpha_2) \quad (22)$$

$$r_{d3} = (-L_1 \frac{\alpha_2}{\alpha_1} \frac{1}{C} - L_1 \frac{\alpha_3}{\alpha_1} \frac{r_2}{L_2} + k \frac{L_1}{\alpha_1} \alpha_3) \quad (23).$$

Note that, using the determined new three controller parameters to solve the original sliding surface function parameters and the gain of reaching law, we can obtain an infinite number of solutions. Thus, the sliding surface function parameters and the gain of reaching law must exist. As long as the sliding surface passes through the origin, the system would converge to the origin, where the Lyapunov stability of PWM-SMC is not affected.

Therefore, a new control law can be derived as

$$u_i = L_1 \dot{d}_e + r_{d1} x_{e1} + r_{d2} x_{e2} + r_{d3} x_{e3} \quad (24).$$

However, in a practical system, *LCL* filter parameters and parasitic resistances have tolerances. L_1 , L_2 , C , r_1 and r_2 represent the actual parameters of system, while \hat{L}_1 , \hat{L}_2 , \hat{C} , \hat{r}_1 and \hat{r}_2 represent the estimated parameters, respectively. There is a deviation between the actual parameter and the estimated one, and the *LCL* filter parameters used in the PWM-SMC controller are the estimated parameter. According to [29], this deviation would cause the steady-state error of system, where the multiple resonant terms can effectively eliminate it. Therefore, in our case, a PR term is instead of the gain of r_{d3} , and the transfer function is,

$$G_c(s) = k_p + \frac{2k_r \omega_i s}{s^2 + 2\omega_i s + \omega_0^2} \quad (25)$$

where k_p and k_r are the proportional and resonant gains, and ω_i and ω_0 are the cutoff frequency and the fundamental frequency, respectively.

Due to the adoption of digital control, it is necessary to consider the delay issue after obtaining the control law. T_s is the sampling period. The zero-order hold is

$$G_{zoh}(s) = \frac{1 - e^{-T_s s}}{s} \quad (26).$$

Thus, when a T_s computation delay is addressed, the total delay $G_d(s)$ is

$$G_d(s) = \frac{1}{T_s} e^{-T_s s} G_{zoh}(s) \approx e^{-1.5T_s s} \quad (27).$$

Thus, the whole control block diagram of proposed design of SMC controller using linearized model can be drawn in Fig. 5.

The closed-loop transfer function is

$$G(s) = \frac{I_2(s)}{I_2^*(s)} = \frac{a_5 s^5 + a_4 s^4 + a_3 s^3 + a_2 s^2 + a_1 s + a_0}{b_5 s^5 + b_4 s^4 + b_3 s^3 + b_2 s^2 + b_1 s + b_0} \quad (28),$$

where

$$a_5 = C_f \hat{L}_1 \hat{L}_2$$

$$a_4 = C_f \hat{L}_1 \hat{r}_2' + C_f \hat{L}_2 \hat{r}_1' + C_f \hat{L}_2 \hat{r}_{d1}' + 2C_f \hat{L}_1 \hat{L}_2 \omega_i$$

$$a_3 = C_f \hat{L}_1 \hat{L}_2 \omega_0^2 + \hat{L}_1 + \hat{L}_2 + \hat{L}_2 \hat{r}_{d2}' + C_f \hat{r}_1' \hat{r}_2' \\ + C_f \hat{r}_2' \hat{r}_{d1}' + 2C_f \hat{L}_1 \hat{r}_2' \omega_i + 2C_f \hat{L}_2 \hat{r}_1' \omega_i + 2C_f \hat{L}_2 \hat{r}_{d1}' \omega_i$$

$$a_2 = k_p + \hat{r}_1' + \hat{r}_2' + \hat{r}_{d1}' + 2\hat{L}_1 \omega_i + 2\hat{L}_2 \omega_i + \hat{r}_2' \hat{r}_{d2}' \\ + 2\hat{L}_2 \hat{r}_{d2}' \omega_i + C_f \hat{L}_1 \hat{r}_2' \omega_0^2 + C_f \hat{L}_2 \hat{r}_1' \omega_0^2 + C_f \hat{L}_2 \hat{r}_{d1}' \omega_0^2 \\ + 2C_f \hat{r}_1' \hat{r}_2' \omega_i + 2C_f \hat{r}_2' \hat{r}_{d1}' \omega_i$$

$$a_1 = 2k_p \omega_i + 2k_r \omega_i + 2\hat{r}_1' \omega_i + 2\hat{r}_2' \omega_i \\ + 2\hat{r}_{d1}' \omega_i + \hat{L}_1 \omega_0^2 + \hat{L}_2 \omega_0^2 + 2\hat{L}_1 \omega_i + 2\hat{L}_2 \omega_i \\ + 2\hat{r}_2' \hat{r}_{d2}' \omega_i + \hat{L}_2 \hat{r}_{d2}' \omega_0^2 + C_f \hat{r}_1' \hat{r}_2' \omega_0^2 + C_f \hat{r}_2' \hat{r}_{d1}' \omega_0^2$$

$$a_0 = k_p \omega_0^2 + \hat{r}_1' \omega_0^2 + \hat{r}_2' \omega_0^2 + \hat{r}_{d1}' \omega_0^2 + \hat{r}_2' \hat{r}_{d2}' \omega_0^2$$

$$b_5 = C_f \hat{L}_1 \hat{L}_2 e^{1.5s \cdot T_s}$$

$$b_4 = C_f \hat{L}_2 \hat{r}_{d1}' + C_f \hat{L}_1 \hat{r}_2' e^{1.5s \cdot T_s} + C_f \hat{L}_2 \hat{r}_1' e^{1.5s \cdot T_s} + 2C_f \hat{L}_1 \hat{L}_2 \omega_i e^{1.5s \cdot T_s}$$

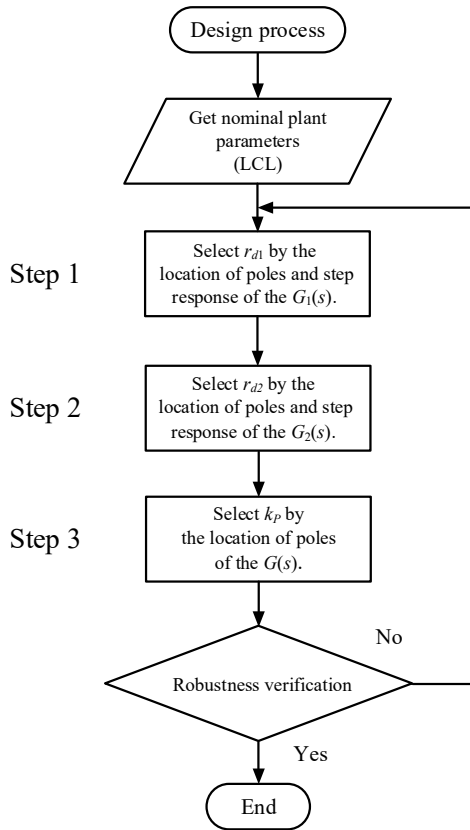


Fig. 6. Proposed design flowchart.

$$\begin{aligned}
 b_3 &= C_f L_1 L_2 e^{1.5sT_s} \omega_o^2 + L_2 r_{d2} + L_1 e^{1.5sT_s} \\
 &\quad + L_2 e^{1.5sT_s} + C_f r_2 r_{d1} + C_f r_1 r_2 e^{1.5sT_s} + 2C_f L_2 r_{d1} \omega_i \\
 &\quad + 2C_f L_1 r_2 \omega_i e^{1.5sT_s} + 2C_f L_2 r_1 \omega_i e^{1.5sT_s} \\
 b_2 &= k_p + r_{d1} + r_2 r_{d2} + r_1 e^{1.5sT_s} + r_2 e^{1.5sT_s} + 2L_2 r_{d2} \omega_i \\
 &\quad + 2L_1 \omega_i e^{1.5sT_s} + 2L_2 \omega_i e^{1.5sT_s} + C_f L_2 r_{d1} \omega_o^2 + 2C_f r_2 r_{d1} \omega_i \\
 &\quad + 2C_f r_1 r_2 \omega_i e^{1.5sT_s} + C_f L_1 r_2 \omega_o^2 e^{1.5sT_s} + C_f L_2 r_1 \omega_o^2 e^{1.5sT_s} \\
 b_1 &= 2k_p \omega_i + 2k_r \omega_i + 2r_{d1} \omega_i + L_1 \omega_o^2 e^{1.5sT_s} \\
 &\quad + L_2 \omega_o^2 e^{1.5sT_s} + 2r_2 r_{d2} \omega_i + 2r_1 \omega_i e^{1.5sT_s} + 2r_2 \omega_i e^{1.5sT_s} \\
 &\quad + L_2 r_{d2} \omega_o^2 + C_f r_2 r_{d1} \omega_o^2 + C_f r_1 r_2 \omega_o^2 e^{1.5sT_s} \\
 b_0 &= k_p \omega_o^2 + r_1 \omega_o^2 e^{1.5sT_s} + r_2 \omega_o^2 e^{1.5sT_s} + r_{d1} \omega_o^2 + r_2 r_{d2} \omega_o^2.
 \end{aligned}$$

As shown in Fig. 5, although compared with the conventional SMC control law, the reconstructed SMC control law has been simplified, there are still three cascaded control loops and three feedforward terms in our control diagram. It is still a big challenge for engineers to design the controller.

Here, a three-loop step-by-step design procedure will be introduced. The design flowchart is shown in Fig. 6. Firstly, based on the nominal *LCL* filter parameters ($L_1 = 1.2$ mH, $L_2 = 1.2$ mH and $C = 6$ μ F), the inner inverter-side current loop is designed and the controller parameter r_{d1} is selected. Secondly, based on the previous controller parameter r_{d1} , the middle loop of capacitor voltage feedback is designed and the controller parameter r_{d2} is chosen. Thirdly, the outer PR controller is designed, according to the previous controller parameters r_{d1} and r_{d2} . Finally, the verification of robustness

against *LCL* filter parameters drift is addressed, after selecting the controller parameters.

It is worth mentioning that the following method can get the approximate stability regions of the inner and middle loop. The outer loop would ultimately determine the stability of the system. Due to the complexity of the control diagram, through this design procedure, only a set of better parameters can be obtained, but the optimal controller parameters is hardly chosen. During the stability analysis, the sample frequency is set as 12 kHz, which is equal to the switching frequency.

B. Step-by-step Parameters Tuning

Step 1-Design the Gain r_{d1}

The control block diagram of the inverter-side current loop is shown in Fig. 7. Here, the reference and the feedback of capacitor voltage are both regarded as perturbation terms. The closed-loop transfer function is

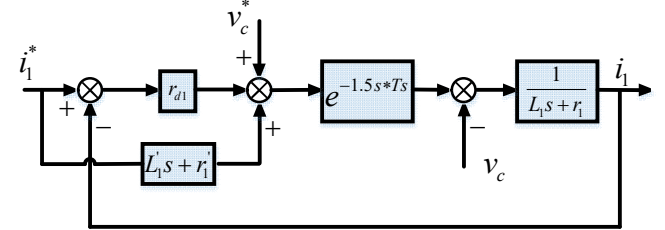


Fig. 7. Block diagram of the inverter-side current loop.

$$G_1(s) = \frac{i_1(s)}{i_1^*(s)} = \frac{L_1 s + r_1 + r_{d1}}{(L_1 e^{1.5sT_s})s + r_{d1} + r_1 e^{1.5sT_s}} \quad (29)$$

In order to facilitate the observation of the location of the poles and improve the accuracy of the digital realization, the transfer function in the above continuous domain is linearly discretized by MATLAB. Fig. 8 shows the discrete closed-loop pole locations of (29). It can be seen that the poles are located inside the unit circle, as long as the gain r_{d1} less than 12.

In order to assist with selecting the value of r_{d1} , the step responses of $G_1(s)$ with different r_{d1} are illustrated in Fig. 9, where the preferred region of r_{d1} range is between 3 and 6. Here, the r_{d1} is chosen as 4.

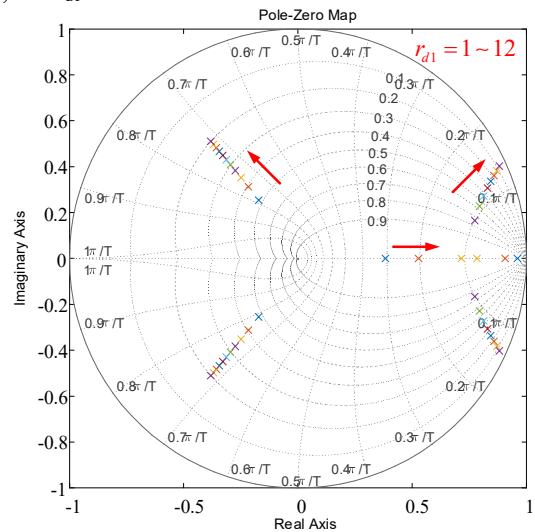


Fig. 8. Closed-loop pole locations of $G_1(s)$, when r_{d1} varies from 1 to 12.

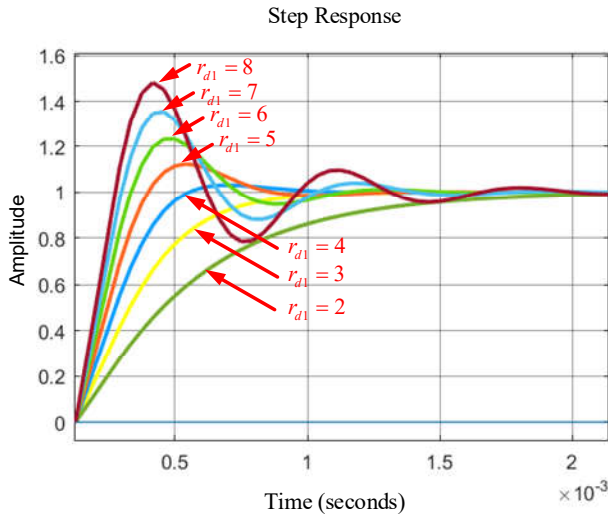


Fig. 9. Step responses of $G_1(s)$ with different r_{d1} .

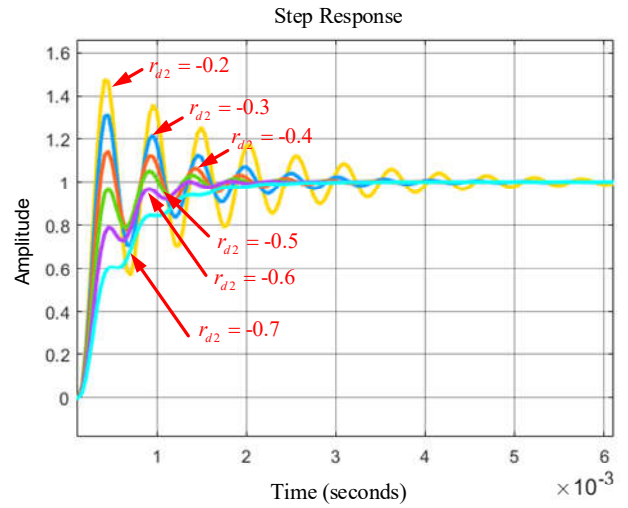


Fig. 12. Step responses of $G_2(s)$ with different r_{d2} .

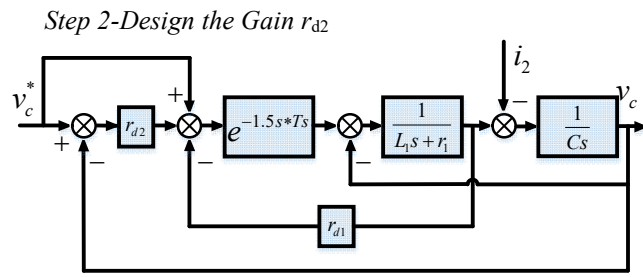


Fig. 10. Block diagram of the capacitor voltage loop.

The design of r_{d2} is similar to that of r_{d1} . The diagram of the middle loop of capacitor voltage feedback is depicted in Fig. 10, where the inverter-side current reference and the grid-injected current feedback are regarded as disturbance terms. The closed-loop transfer function is

$$G_2(s) = \frac{v_c(s)}{v_c^*(s)} = \frac{1 + r_{d2}}{(CL_1 e^{1.5sT_s})s^2 + (Cr_{d1} + Cr_1 e^{1.5sT_s})s + r_{d2} + e^{1.5sT_s}} \quad (30)$$

Fig. 11 shows the closed-loop pole locations of $G_2(s)$, showing that the stable region of r_{d2} ranges from -0.9 to -0.2. This is an approximate range of stability region, mainly to avoid introducing unstable poles.

Similarly, the step responses of $G_2(s)$ with different r_{d2} are illustrated in Fig. 12. Here, r_{d2} is chosen as -0.4.

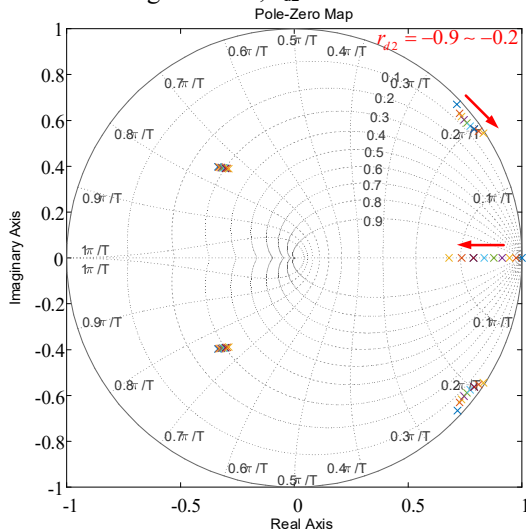


Fig. 11. Closed-loop pole locations of $G_2(s)$, when r_{d2} varies from -0.9 to -0.2.

Step 3-Design the Proportional Gain k_p

Although the PR controller is adopted, the stability of system mainly depends on the proportional term of k_p , since the resonant frequency is 50 Hz and the desired control bandwidth is far higher than 50 Hz. Therefore, the PR controller is simplified as k_p .

With r_{d1} and r_{d2} the closed-loop pole locations of $G(s)$ are shown in Fig. 13, where it can be clearly seen that the stable region of k_p is between 1 to 12 and the critical value of k_p is about 13. Finally, k_p is selected as 10 to ensure sufficient control bandwidth and stable margin. The resonant term of k_r is just selected as an initial value. In our case, k_r is chose as 800. In particular, according to the actual situation, the harmonic compensators could be inserted into the PR controller to resist the low order current harmonics caused by background harmonic voltages.

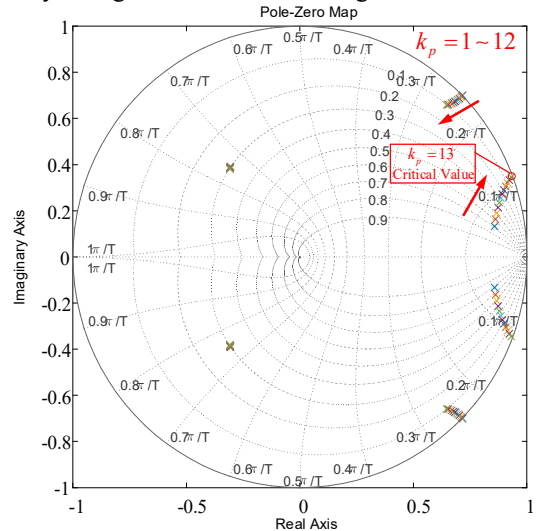


Fig. 13. Closed-loop pole locations of $G(s)$, when k_p varies from 1 to 12.

C. Robustness Analysis against Parameters Drift

Let the parameters of the LCL filter vary in a wide range. L_1 varies in the range of 0.8 mH-2.0 mH (-33%~+66% of L_1), C varies in the range of 4 uF-9 uF (-33%~+50% of C), and the grid side inductance L_g varies in the range of 0 mH-6 mH (0%~+500% of L_2), respectively. Then the locations of the closed-loop poles of the system are derived. If the closed-loop poles of $G(s)$ are still located inside the unit

IEEE POWER ELECTRONICS REGULAR PAPER/LETTER/CORRESPONDENCE

circle, the system is stable, which means that the controller parameter is reasonable and feasible. If any closed-loop pole locations of the system are located outside the unit circle, the system is unstable. Then, we have to go back to redesign the gains of r_{d1} , r_{d2} , and k_p , and then test the robustness again. From Fig. 14, it can be clearly seen that all the closed-loop poles of $G(s)$ are still located inside the unit circle when the parameters of the LCL filter vary in a wide range.

In order to further evaluate the robustness of the proposed control strategy, a comparison between the traditional capacitor-current-feedback active damping (AD) method and the proposed method is performed. Notably, if the resonance frequency is equal to one-sixth of the sampling frequency and the total delay time is equal to one and half sampling period, the system can be hardly stable, no matter how much the capacitor-current-feedback coefficient is [37]. Here, the LCL parameters are set as $L_1=1.6$ mH, $L_2=1.2$ mH, $L_g=1.9$ mH and $C=6$ μ F, where the resonance frequency is about 2000 Hz ($f_s/6$). As shown in Fig. 15, some closed-loop poles of $G(s)$ with the traditional AD method are always located on the unit circle or outside the unit circle with various capacitor-current-feedback coefficients, while the closed-loop poles of $G(s)$ with the proposed control strategy are all located inside the unit circle. It can be clearly proven that the proposed control strategy has a better stable region than the traditional capacitor-current-feedback AD method.

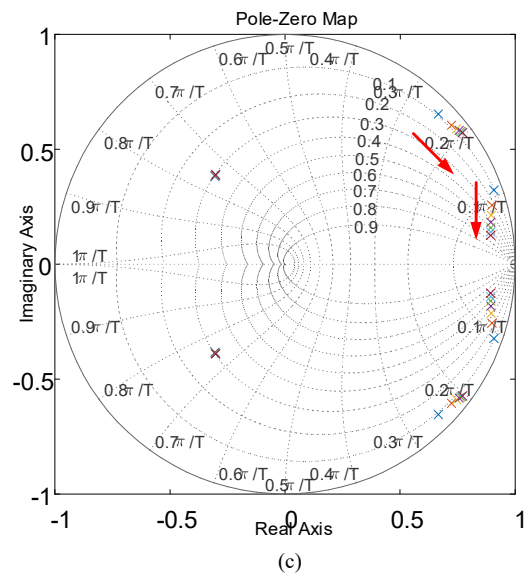
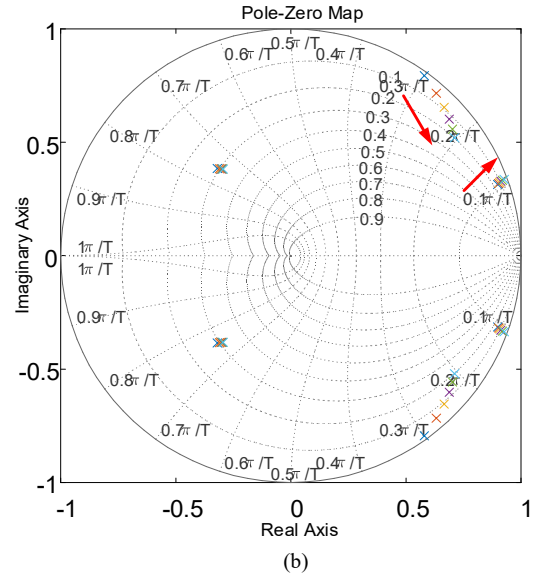
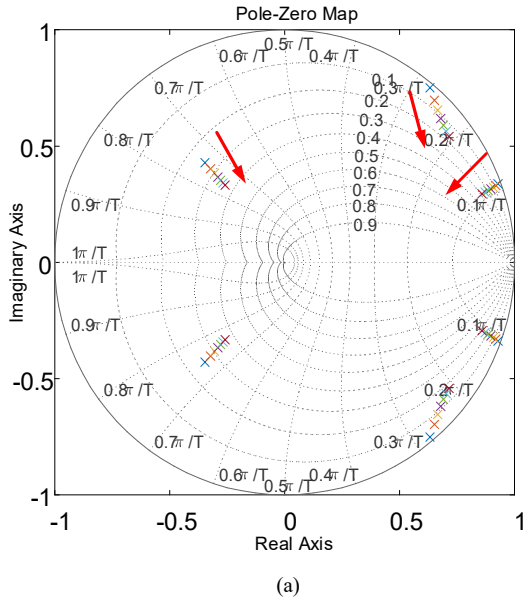


Fig. 14. Closed-loop pole locations of $G(s)$ when the filter parameter varies. (a) L_1 varies in the range of 0.8 mH-2.0 mH. (b) C varies in the range of 4 uF-9 uF. (c) L_g varies in the range of 0 mH-6 mH.

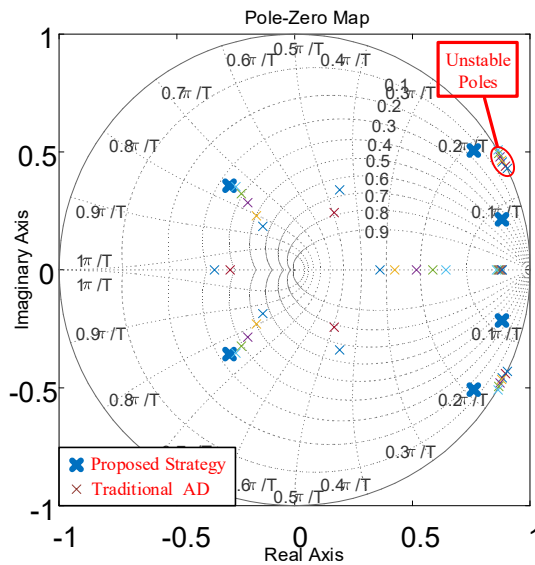


Fig. 15. Closed-loop pole locations of $G(s)$ with traditional AD method and proposed control strategy when the resonance frequency is about 2000 Hz ($f_s/6$).

V. BRIEF DESIGN OF DISCRETE STATE OBSERVER

In order to save the total sensors, a simple and easily implemented discrete state observer is also adopted.

Based on (1)-(6), the discrete model of the system is obtained as

$$x(k+1) = A_d x(k) + B_d u_i(k) + D_d v_g(k) \quad (31)$$

$$A_d = \begin{bmatrix} 1 - \frac{r_1 T_s}{L_1} & -\frac{T_s}{L_1} & 0 \\ \frac{T_s}{C_f} & 1 & -\frac{T_s}{C_f} \\ 0 & \frac{T_s}{L_2} & 1 - \frac{r_2 T_s}{L_2} \end{bmatrix} B_d = \begin{bmatrix} \frac{T_s V_{dc}}{L_1} \\ 0 \\ 0 \end{bmatrix} C_d = \begin{bmatrix} 0 \\ 0 \\ 1 \end{bmatrix} D_d = \begin{bmatrix} 0 \\ 0 \\ \frac{T_s v_{pcc}}{L_2} \end{bmatrix}$$

As shown in Fig. 16, the discrete state observer is given by

$$\begin{cases} \hat{x}(k+1) = A_d \hat{x}(k) + B_d u_i(k) + D_d v_g(k) + L_d [\hat{y}(k) - y(k)] \\ \hat{y}(k) = C_d \hat{x}(k) \end{cases} \quad (32)$$

where the subscript “” denotes the estimated value, L_d is the observer gain vector.

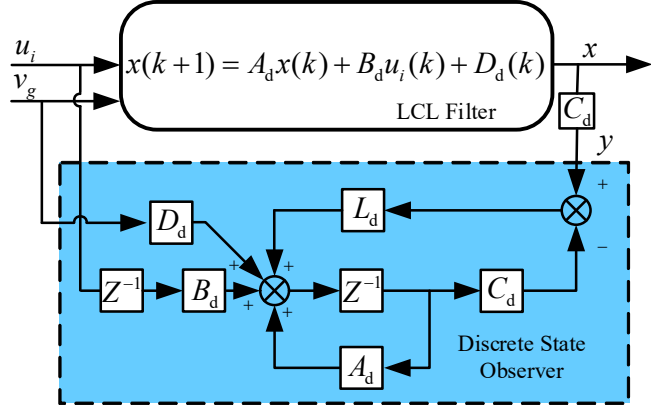


Fig. 16. Structure of the discrete state observer.

The design of L_d is carried out via zero pole assignment. The poles of the closed-loop system consist of the union of the controller poles and the observer poles. A rule of thumb is to select the observer poles to be two to six times faster than the poles of the controller. Then, the observer dynamics do not limit the bandwidth determined by the controller.

Generally, if the poles of the observer are chosen as three to five times faster than those of the controller, the dynamic characteristics of the observer will not impose any restrictions on the bandwidth determined by the controller. However, the observer's poles should not exceed the Nyquist frequency.

The characteristic polynomial of the observer dynamics is selected as

$$\det(zI_3 - G + L_d C_d) = (z - p_1)(z - p_2)(z - p_3) \quad (33)$$

where p_1 , p_2 and p_3 are the desired poles of observer, then observer gain vector can be calculated.

According to the principle of separation, the design of state observer and current controller do not affect each other, which means the sliding mode controller and the state observer can be designed independently.

VI. EXPERIMENTAL VERIFICATIONS

In order to validate the effectiveness of the proposed strategy, a prototype of 3 kW three-phase three-wire LCL-filter-based system with proposed control scheme has been implemented by using the DSpace DS1202. When constructing the control loop, the control law is discretized due to the digital implementation. The power grid is emulated with Chroma 61830. Yokogawa DL 1640 digital oscilloscope is used to measure the grid voltage waveform and grid-injected current waveform. The experimental setup is shown in Fig. 17, while the system parameters and nominal controller parameters are listed in TABLE I.

TABLE I
SYSTEM PARAMETERS

Symbol	Value	Symbol	Value
Grid voltage v_g	110 V(RMS)	Switching frequency f_{sw}	12 kHz
DC link voltage U_{dc}	350 V	Sampling frequency f_s	12 kHz
Inverter-side inductor L_1	1.2 mH	Coefficient of control k_p	10
Grid-side inductor L_2	1.2 mH	Coefficient of control k_r	800
Filter capacitor C	6 μ F	Coefficient of control k_{d1}	4
Equivalent series resistance of L_1	0.2 Ω	Coefficient of control k_{d2}	-0.4
Equivalent series resistance of L_2	0.2 Ω		

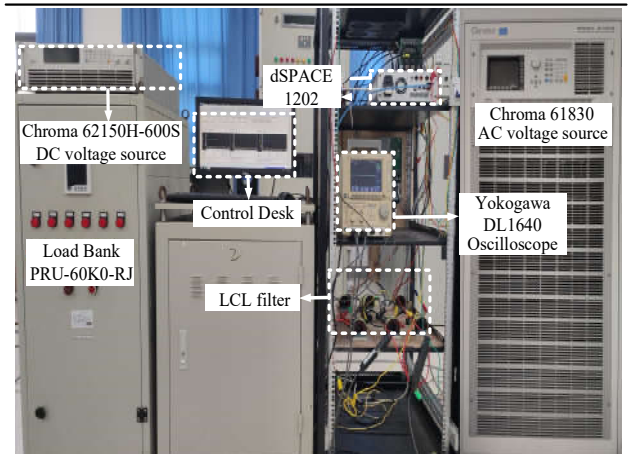


Fig. 17. Experimental setup.

A. Performance under Nominal LCL Parameters Condition

Fig. 18 and Fig. 19 show the results under nominal LCL parameters condition.

Fig. 18 shows that the grid-injected current can keep tracking the reference with zero steady-state error when $k_p=10$. In addition, the grid-injected current steps down from 12.86 A to 6.43 A, where the proposed strategy exhibits a fast dynamic response, meaning that the system has achieved a wide control bandwidth.

While, Fig. 19 shows that the measured grid voltage and grid-injected current oscillated, when the gain k_p increased to 13 (critical value obtained by theory analysis), which matches the theoretical analysis in Fig. 13 quite well.

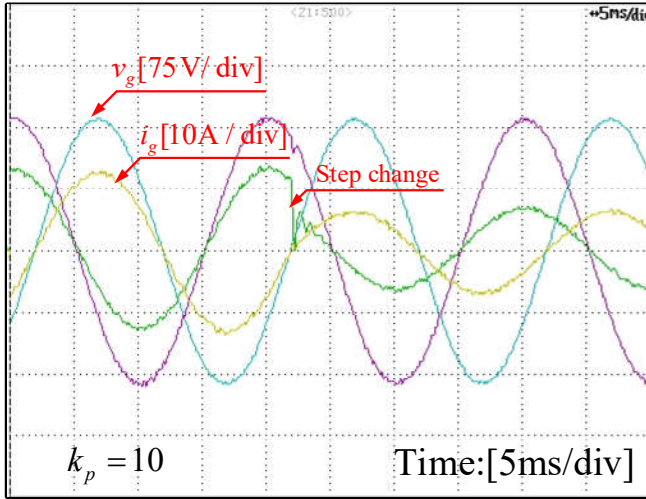


Fig. 18. Measured grid voltage waveform and grid-injected current waveform when $k_p=10$.

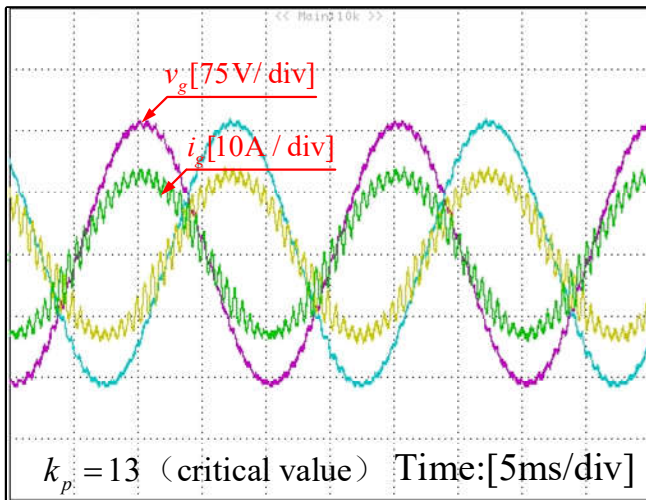


Fig. 19. Measured grid voltage waveform and grid-injected current waveform when $k_p=13$.

B. Performance under LCL Filter Parameters Drift Condition

To evaluate the robustness of the proposed control strategy, Fig. 20, Fig. 21 show the grid-injected current under the condition of LCL filter parameters drift (L_1 varies -33%, C varies -33% from the nominal values, respectively). Despite of the variations of LCL filter parameters, the system can still be stable and achieve zero steady-state error, which is good agreement with the closed-loop pole locations of $G(s)$ in Fig. 14.

In actual applications, the grid inductance may change in a large range, especially when multiple GCIs are in parallel connected with the power grid at the same common coupling point [9]. To emulate this situation, the external inductors ($L_g = 6$ mH) are adopted. As shown in Fig. 22, the system remains stable with zero steady-state error. It is worth mentioning that the large equivalent grid impedance usually leads to the decrease of the system control bandwidth. However, the transient response with the proposed control strategy is good (the settling time is within one cycle as shown in Fig. 22), proving that the proposed strategy can also achieve a good control bandwidth.

Fig. 23 shows grid-injected current with the capacitor-current-feedback AD method when the resonance frequency

is about 2000 Hz (fs/6). The system is unstable which is consistent with conclusions in [37]. Fig. 24 shows grid-injected current with the proposed control strategy under the same condition, where the system is stable. It can be proven that the proposed control strategy has a wider stable region than that with the conventional capacitor-current-feedback AD method.

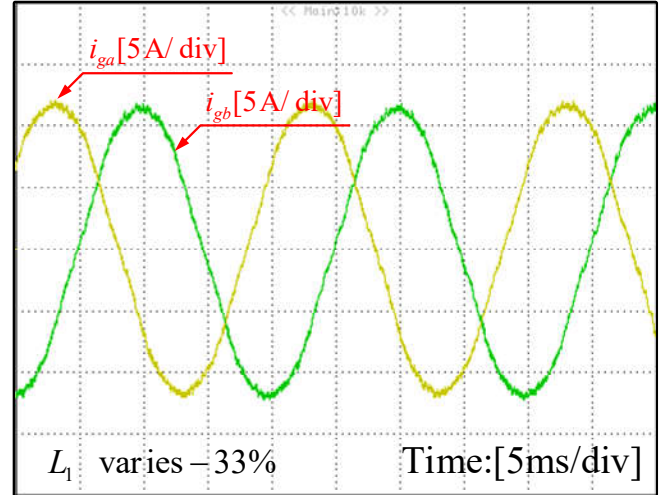


Fig. 20. Measured grid-injected current waveform when $L_1 = 0.8$ mH, $L_2+L_g = 1.2$ mH, and $C = 6$ μ F.

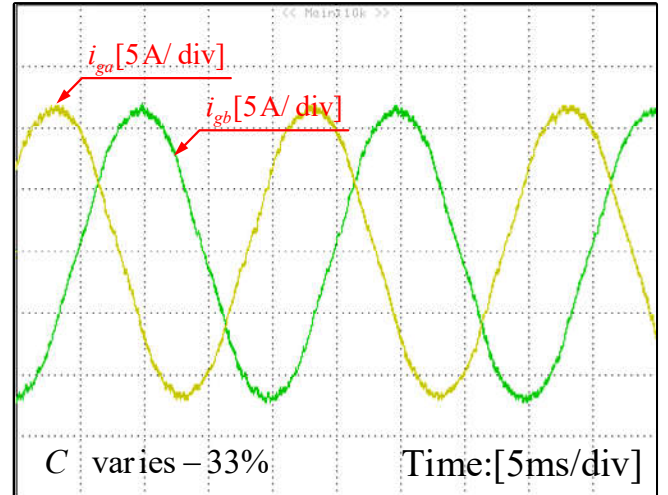


Fig. 21. Measured grid-injected current waveform when $L_1 = 1.2$ mH, $L_2+L_g = 1.2$ mH, and $C = 4$ μ F.

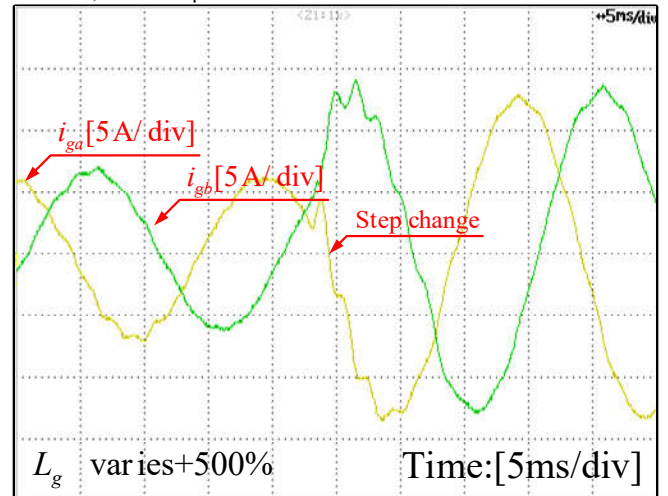


Fig. 22. Dynamic performance when $L_1 = 1.2$ mH, $L_2+L_g = 7.2$ mH, and $C = 6$ μ F.

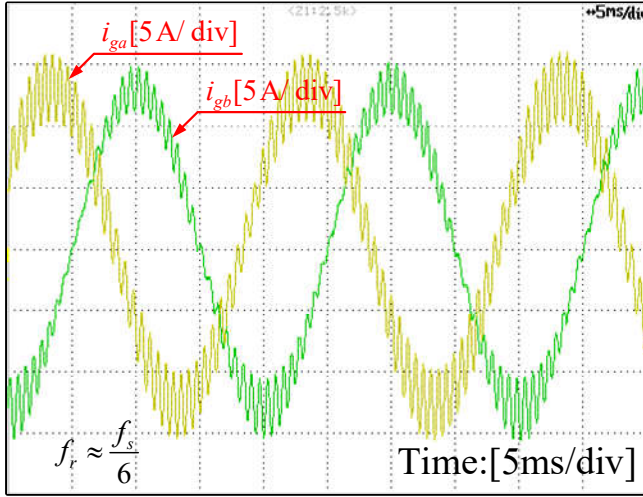


Fig. 23. Measured grid-injected current waveform with the capacitor-current-feedback AD when the resonance frequency is about 2000 Hz ($f_r \approx f_s/6$).

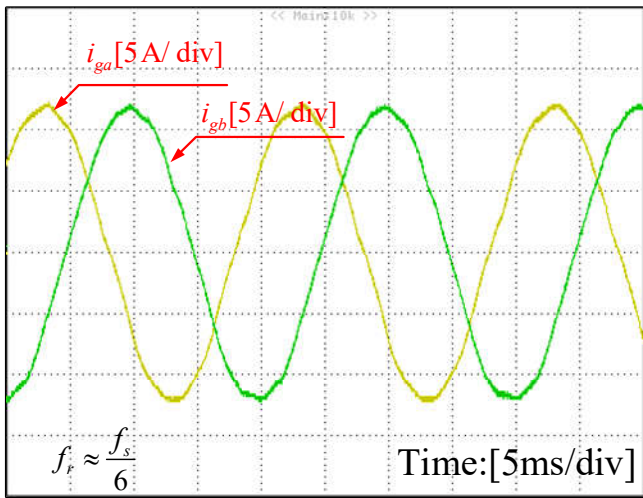


Fig. 24. Measured grid-injected current waveform with the proposed control strategy when the resonance frequency is about 2000 Hz ($f_r \approx f_s/6$).

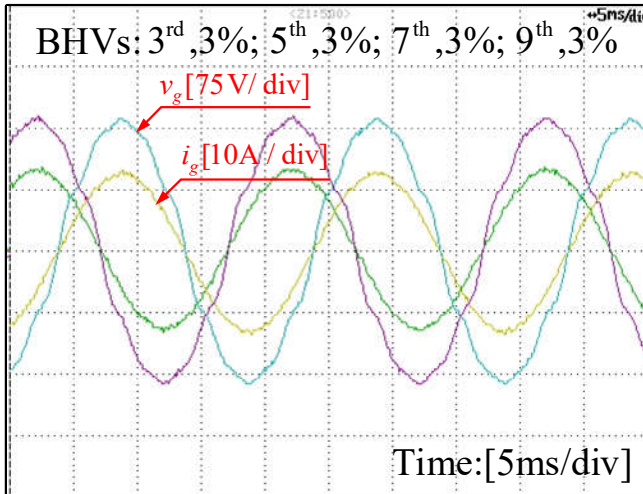


Fig. 25. Measured grid voltage waveform and grid-injected current waveform under a distorted grid.

C. Performance under a Distorted Grid

Fig. 25 shows the measured grid-injected current and grid voltage under a distorted grid. A programmable AC

source (Chroma 61830) is utilized to emulate the grid voltage, which is distorted by the 3rd, 5th, 7th, 9th harmonics. The magnitudes of harmonics with respect to the grid fundamental voltage are 3%, 3%, 3% and 3%, respectively. Due to the PR term and the wide bandwidth of the system, the grid-injected current remains sinusoidal, which proves the proposed system has the strong ability to resist the adverse effect caused by the harmonic grid voltage.

VII. DISCUSSION

A. Comparison with the Existing SMC Methods

Through the experimental results, it can be observed that the proposed design guideline of robust PWM-SMC controller is practical. A summary of comparison between the existing SMC methods and the proposed SMC strategy is shown in Table II. The performance of the system is analyzed from the following perspectives: sampling frequency, switching frequency, number of measured state variables, power rating, *LCL* filter parameters and harmonic rejection.

1) HM-SMC

In [26], [27] and [28], the hysteresis modulator is utilized to ensure the switching of the HM-SMC system. The width of the hysteresis band controls the switching frequency. Among these three cases, there are two obvious advantages: fast dynamic response (which means high control bandwidth) and highly strong robustness. This is mainly because the hysteresis modulator directly realizes the switching of the system, which reflects the invariance of SMC theory. However, the issue of variable switching frequency introduced by the hysteretic modulator will impose a burden on the design of *LCL* filter. For example, in [27] and [28], the total inductance is 7 mH and 12 mH, respectively, which may cost much. In addition, in order to achieve a good control effect, a high sampling frequency is needed. For example, the sampling frequency is 125 KHz in [26], which need high requirements for digital control.

Compared with the above HM-SMC methods, the proposed control strategy adopts the pulse width modulation, where the switching frequency is fixed and the sampling frequency is low. Thus, the total inductance is 2.4 mH and the sampling frequency is 12 kHz. Although the dynamic response is not so fast as the one with HM-SMC, the experiment results show that the transient performance is acceptable.

2) PWM-SMC

In [29] and [30], the PWM-SMC is used for controller design, where the Lyapunov stability theorem is utilized to verify the stability of the system. However, this theorem cannot obtain the accurate stability region. Thus, in [29] and [30], the design of SMC controller parameters had not been presented in detail.

Compared with the above PWM-SMC methods, the proposed control strategy analyzes the essence of the SMC and then provides an accurate and detailed design guideline, which can help engineers to precisely design a highly robust PWM-SMC controller.

TABLE II
COMPARISONS BETWEEN THE EXISTING SMC METHODS AND THE PROPOSED ONE

		HM-SMC			PWM-SMC		
Comparison category		[26]	[27]	[28]	[29]	[30]	Proposed
Sampling frequency		125 kHz	60 kHz	40 kHz	15 kHz	12 kHz	12 kHz
Switching frequency		18.8 kHz	6 kHz	6 kHz	15 kHz	12 kHz	12 kHz
Measured variables		3	2	2	4	4	2
Power Rating		3.3 kW	1.5 kW	1.5 kW	5 kW	3.2 kW	3 kW
LCL filter	L_1	1.74 mH	5 mH	7 mH	1.2 mH	1 mH	1.2 mH
	C	50 μ F	6.8 μ F	6.8 μ F	50 μ F	62 μ F	6 μ F
	L_2	0.6867 mH	2 mH	5 mH	0.4 mH	0.3 mH	1.2 mH
Harmonic rejection		Not reported	Good	Good	Good	Not reported	Good

In addition, the performance of the proposed PWM-SMC strategy is satisfactory, including the robustness, harmonic rejection and steady-state error. Owing to the implementation of discrete state observer, only two state variables are measured.

B. Comparison with the Full-state Feedback Controller

It is worth mentioning that the proposed PWM-SMC strategy utilized three state variables, which is in the same way as the full-state feedback controller. Indeed, from the perspective of digital implementation, there is a little similarity between the two control methods.

However, from the perspective of the physical significance, the two control methods are totally different. The SMC strategy provides a nonlinear view on the control of the power electronics, where the physical significance, for example as shown in Figs 2 and 4, is much more clear.

Further, in the proposed PWM-SMC control law, there are some feedforward terms, which can have some effects on improving the dynamic response and eliminating the steady-state error. However, since the lack of the global system modeling, the full-state feedback controller does not have these feedforward terms.

VIII. CONCLUSION

This paper presents a novel step-by-step design guideline of robust PWM-SMC controller using linearized model for three-phase GCI with LCL filter. The conclusions can be drawn as following:

- 1) There are many ways to realize switching in SMC system. Hysteresis modulator and pulse width modulator are two special switching modes in power electronics, which can ensure the switching of the system without extra nonlinear term in the control law.
- 2) Compared with the HM-SMC controller, the size of output filter and the sampling frequency can be much smaller for the proposed strategy.
- 3) Different from the traditional PWM-SMC based on Lyapunov stability or phase plane, the proposed strategy has adopted the linear tool to design SMC parameters, where the accurate stability region can be exactly obtained, especially when the delay issue is addressed.

A 3 kW/3-phase/110 V experimental lab setup has been constructed to verify the feasibility of proposed PWM-SMC controller using linearized model design strategy. The experimental results show that the proposed PWM-SMC controller has the excellent robustness against the filter parameters shift and satisfactory dynamic performance, even under the condition of seriously distorted grid.

IX. REFERENCES

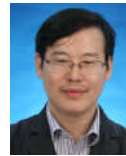
- [1] F. Blaabjerg, R. Teodorescu, M. Liserre, and A. V. Timbus, "Overview of control and grid synchronization for distributed power generation systems," *IEEE Trans. Ind. Electron.*, vol. 53, no. 5, pp. 1398–1409, Oct. 2006.
- [2] W. Wu, Y. He and F. Blaabjerg, "An LLCL Power Filter for Single-Phase Grid-Tied Inverter," *IEEE Trans. Power Electron.*, vol. 27, no. 2, pp. 782–789, Feb. 2012.
- [3] R. Peña-Alzola, M. Liserre, F. Blaabjerg, R. Sebastián, J. Dannehl and F.W. Fuchs, "Analysis of the passive damping losses in LCL-filter-based grid converters," *IEEE Trans. Power Electron.*, vol. 28, no. 6, pp.2642–2646, June 2013.
- [4] W. Wu, Y. He, T. Tang and F. Blaabjerg, "A new design method for the passive damped LCL and LLCL filter-based single-phase grid-tied inverter," *IEEE Trans. Ind. Electron.*, vol. 60, no. 10, pp. 4339–4350, Oct.2013.
- [5] Z. Bai, H. Ma, D. Xu, B. Wu, Y. Fang, and Y. Yao, "Resonance damping and harmonic suppression for grid-connected current-source inverter," *IEEE Trans. Ind. Electron.*, vol. 61, no. 7, pp. 3146–3154, Jul. 2014.
- [6] R. Peña-Alzola, M. Liserre, F. Blaabjerg, M. Ordóñez and T. Kerekes, "A Self-commissioning Notch Filter for Active Damping in a Three-Phase LCL -Filter-Based Grid-Tie Converter," *IEEE Trans. Power Electron.*, vol. 29, no. 12, pp. 6754–6761, Dec. 2014.
- [7] Y. Liu, W. Wu, Y. He, Z. Lin, F. Blaabjerg and H. S. H. Chung, "An efficient and robust hybrid damper for LCL- or LLCL-based grid-tied inverter with strong grid-side harmonic voltage effect rejection," *IEEE Trans. Ind. Electron.*, vol. 63, no. 2, pp. 926–936, Feb. 2016.
- [8] M. Ben Saïd-Romdhane, M. W. Naouar, I. Slama-Belkhdja and E. Monmasson, "Robust Active Damping Methods for LCL Filter-Based Grid-Connected Converters," *IEEE Trans. Power Electron.*, vol. 32, no. 9, pp. 6739–6750, Sept. 2017.
- [9] W. Wu, Y. Liu, Y. He, H. S. H. Chung, M. Liserre and F. Blaabjerg, "Damping methods for resonances caused by LCL-filter-based current-controlled grid-tied power inverters: an overview," *IEEE Trans. Ind. Electron.* vol. 64, no. 9, pp. 7402–7413, Sept. 2017.
- [10] L. Jia, X. Ruan, W. Zhao, Z. Lin and X. Wang, "An Adaptive Active Damper for Improving the Stability of Grid-Connected Inverters Under Weak Grid," *IEEE Trans. Power Electron.*, vol. 33, no. 11, pp. 9561–9574, Nov. 2018.
- [11] J. Roldán-Pérez, E. J. Bueno, R. Peña-Alzola and A. Rodríguez-Cabero, "All-Pass-Filter-Based Active Damping for VSCs With LCL Filters Connected to Weak Grids," *IEEE Trans. Power Electron.*, vol. 33, no. 11, pp. 9890–9901, Nov. 2018.

IEEE POWER ELECTRONICS REGULAR PAPER/LETTER/CORRESPONDENCE

- [12] Z. Zhang, W. Wu, Z. Shuai, X. Wang, "Principle and robust impedance-based design of grid-tied inverter with LLCL-Filter under wide variation of grid-reactance," *IEEE Trans. Power Electron.*, In press, 2018.
- [13] J. A. Rothen et al., "Model Predictive Control for Power Converters in a Distorted Three-Phase Power Supply," *IEEE Trans. Ind. Electron.*, vol. 63, no. 9, pp. 5838-5848, Sept. 2016.
- [14] N. Panten, N. Hoffmann and F. W. Fuchs, "Finite Control Set Model Predictive Current Control for Grid-Connected Voltage-Source Converters With LCL Filters: A Study Based on Different State Feedbacks," *IEEE Trans. Power Electron.*, vol. 31, no. 7, pp. 5189-5200, July 2016.
- [15] S. Bayhan, M. Trabelsi, H. Abu-Rub and M. Malinowski, "Finite-Control-Set Model-Predictive Control for a Quasi-Z-Source Four-Leg Inverter Under Unbalanced Load Condition," *IEEE Trans. Ind. Electron.*, vol. 64, no. 4, pp. 2560-2569, April 2017.
- [16] S. R. Mohapatra and V. Agarwal, "Model Predictive Controller with Reduced Complexity for Grid Tied Multilevel Inverters," *IEEE Trans. Ind. Electron.*, Accepted, 2018.
- [17] H. Komurcugil, N. Altin, S. Ozdemir and I. Sefa, "Lyapunov-Function and Proportional-Resonant-Based Control Strategy for Single-Phase Grid-Connected VSI With LCL Filter," *IEEE Trans. Ind. Electron.*, vol. 63, no. 5, pp. 2838-2849, May 2016.
- [18] Y. Gui, B. Wei, M. Li, J. M. Guerrero, J. C. Vasquez, "Passivity-based coordinated control for islanded AC microgrid," *Applied Energy*, Vol. 229, pp. 551-561, 2018.
- [19] Y. Chen, M. Wen, E. Lei, X. Yin, J. Lai, Z. Wang, "Passivity-based control of cascaded multilevel converter based D-STATCOM integrated with distribution transformer," *Electric Power Systems Research*, Vol. 154, pp 1-12, Jan. 2018.
- [20] X. Mu, J. Wang, W. Wu and F. Blaabjerg, "A modified multi frequency passivity-based control for shunt active power filter with model-parameter-adaptive capability," *IEEE Trans. Ind. Electron.*, vol. 65, no. 1, pp. 760-769, Jan. 2018
- [21] M. Merai, W. Naouar, I. Slama-Belkhdja and E. Monmasson, "An Adaptive PI Controller Design for DC-Link Voltage Control of Single-Phase Grid-Connected Converters," *IEEE Trans. Ind. Electron.*, Accepted, 2018.
- [22] Z. Zou, G. Buticchi and M. Liserre, "Grid Identification and Adaptive Voltage Control in a Smart Transformer-fed Grid," *IEEE Trans. Power Electron.*, Accepted, 2018.
- [23] D. Martin and E. Santi, "Autotuning of Digital Deadbeat Current Controllers for Grid-Tie Inverters Using Wide Bandwidth Impedance Identification," *IEEE Trans. Ind. Appl.*, vol. 50, no. 1, pp. 441-451, Jan.-Feb. 2014.
- [24] Y. He, H. S. Chung, C. N. Ho and W. Wu, "Modified Cascaded Boundary-Deadbeat Control for a Virtually-Grounded Three-Phase Grid-Connected Inverter With LCL Filter," *IEEE Trans. Power Electron.*, vol. 32, no. 10, pp. 8163-8180, Oct. 2017.
- [25] Y. He, H. S. Chung, C. N. Ho and W. Wu, "Use of Boundary Control With Second-Order Switching Surface to Reduce the System Order for Deadbeat Controller in Grid-Connected Inverter," *IEEE Trans. Power Electron.*, vol. 31, no. 3, pp. 2638-2653, March 2016.
- [26] Hasan Komurcugil, Saban Ozdemir, Ibrahim Sefa, Necmi Altin, and Osman Kukrer, "Sliding mode control for single phase grid connected LCL filtered VSI with double band hysteresis scheme," *IEEE Trans. Ind. Electron.*, vol. 63, no. 2, pp. 864-873, Feb. 2016.
- [27] R. Guzman, L. G. de Vicuña, M. Castilla, J. Miret and J. de la Hoz, "Variable Structure Control for Three-Phase LCL-Filtered Inverters Using a Reduced Converter Model," *IEEE Trans. Ind. Electron.*, vol. 65, no. 1, pp. 5-15, Jan. 2018.
- [28] R. Guzman, L. G. de Vicuña, M. Castilla, J. Miret and H. Martín, "Variable Structure Control in Natural Frame for Three-Phase Grid-Connected Inverters With LCL Filter," *IEEE Trans. Power Electron.*, vol. 33, no. 5, pp. 4512-4522, May 2018.
- [29] X. Hao, X. Yang, T. Liu, L. Huang, and W. Chen, "A sliding-mode controller with multiresonant sliding surface for single-phase grid-connected VSI with an LCL filter," *IEEE Trans. Power Electron.*, vol. 28, no. 5, pp. 2259-2268, May 2013.
- [30] R. P. Vieira, L. T. Martins, J. R. Massing and M. Stefanello, "Sliding mode controller in a multi-loop framework for a grid-connected VSI with LCL filter," *IEEE Trans. Ind. Electron.*, vol. 65, no. 6, pp. 4714-4723, June 2018.
- [31] M. A. E. Alali, Y. B. Shtessel and J. Barbot, "Grid-Connected Shunt Active LCL Control via Continuous Sliding Modes," *IEEE/ASME Trans. Mechatronics*, vol. 24, no. 2, pp. 729-740, April 2019.
- [32] J. Y. Hung, W. Gao and J. C. Hung, "Variable structure control: a survey," *IEEE Trans. Ind. Electron.*, vol. 40, no. 1, pp. 2-22, Feb. 1993.
- [33] Weibing Gao and J. C. Hung, "Variable structure control of nonlinear systems: a new approach," *IEEE Trans. Ind. Electron.*, vol. 40, no. 1, pp. 45-55, Feb. 1993.
- [34] Siew-Chong Tan, Y. M. Lai, C. K. Tse and M. K. H. Cheung, "A fixed-frequency pulsewidth modulation based quasi-sliding-mode controller for buck converters," *IEEE Trans. Power Electron.*, vol. 20, no. 6, pp. 1379-1392, Nov. 2005.
- [35] S. Tan, Y. M. Lai, C. K. Tse, L. Martinez-Salamero and C. Wu, "A Fast-Response Sliding-Mode Controller for Boost-Type Converters With a Wide Range of Operating Conditions," *IEEE Trans. Ind. Electron.*, vol. 54, no. 6, pp. 3276-3286, Dec. 2007.
- [36] A. Abrishamifar, A. Ahmad and M. Mohamadian, "Fixed Switching Frequency Sliding Mode Control for Single-Phase Unipolar Inverters," *IEEE Trans. Ind. Electron.*, vol. 27, no. 5, pp. 2507-2514, May 2012.
- [37] D. Pan, X. Ruan, C. Bao, W. Li and X. Wang, "Optimized Controller Design for SLCL-Type Grid-Connected Inverter to Achieve High Robustness Against Grid-Impedance Variation," *IEEE Trans. Ind. Electron.*, vol. 62, no. 3, pp. 1537-1547, March 2015.



Han Li was born in Anhui Province, China, in 1995. He received the M.S. degree in electrical engineering from Shanghai Maritime University, Shanghai, China, in 2020. His current research interests include sliding mode control, digital control techniques and renewable energy generation systems.



Weimin Wu (M'16) received Ph.D. degrees in Electrical Engineering from the College of Electrical Engineering, Zhejiang University, Hangzhou, China, in 2005. He worked as a research engineer in the Delta Power Electronic Center (DPEC), Shanghai, from July, 2005 to June, 2006. Since July, 2006, he has been a Faculty Member at Shanghai Maritime University, where he is currently a Full Professor in Department of Electrical Engineering. He was a Visiting Professor in the Center for Power Electronics Systems (CPES), Virginia Polytechnic Institute and State University, Blacksburg, USA, from Sept. 2008 to March. 2009. From Nov. 2011 to Jan. 2014, he was also a visiting professor in the Department of Energy Technology, Aalborg University, Denmark, working at the Center of Reliable Power Electronics (CORPE). He has coauthored over 100 papers and holds eight patents. His areas of interests include power converters for renewable energy systems, power quality, smart grid, and energy storage technology. Dr. Wu serves as an Associate Editor for the IEEE TRANSACTIONS ON INDUSTRYELECTRONICS.



Min Huang received the M.S. degree in electrical engineering from Shanghai Maritime University, Shanghai, China, in 2012, and the Ph.D. degree in the Institute of Energy Technology, Aalborg University, Aalborg, Denmark, in 2015. She is currently a Faculty Member at Shanghai Maritime University. Her research interests include power quality, control and power converters for renewable energy systems.



Henry Shu-Hung Chung (M'95-SM'03-F'16) received the B.Eng. and Ph.D. degrees in electrical engineering from the Hong Kong Polytechnic University, Kowloon, Hong Kong, in 1991 and 1994, respectively. Since 1995, he has been with the City University of Hong Kong, Kowloon, where he is currently a Chair Professor in the Department of Electrical Engineering and the Director of the Center for Smart Energy Conversion and Utilization Research. His current research interests include renewable energy conversion technologies, lighting technologies, smart grid

IEEE POWER ELECTRONICS REGULAR PAPER/LETTER/CORRESPONDENCE

technologies, and computational intelligence for power electronic systems. He has edited one book, authored eight research book chapters, and over 460 technical papers including 200 refereed journal papers in his research areas, and holds 50 patents.

Dr. Chung was the Chair of the Technical Committee of the High-Performance and Emerging Technologies, IEEE Power Electronics Society in 2010-2014. He is currently Associate Editor of the IEEE Transactions on Power Electronics and the IEEE Journal of Emerging and Selected Topics in Power Electronics. He was Editor-in-Chief of the IEEE Power Electronics Letters 2014-2018. He has received numerous industrial awards for his invented energy saving technologies.



Marco Liserre (S'00-M'02-SM'07-F'13) received the MSc and PhD degree in Electrical Engineering from the Bari Polytechnic, respectively in 1998 and 2002. He has been Associate Professor at Bari Polytechnic and from 2012 Professor in reliable power electronics at Aalborg University (Denmark). From 2013 he is Full Professor and he holds the Chair of Power Electronics at Kiel University (Germany). He has published 400 technical papers (more than 1/3 of them in international peer-reviewed journals) and a book. These works have received more than 28000 citations. Marco Liserre is listed in ISI Thomson report "The world's most influential scientific minds" from 2014.

He has been awarded with an ERC Consolidator Grant for the project "The Highly Efficient And Reliable smart Transformer (HEART), a new Heart for the Electric Distribution System".

He is member of IAS, PELS, PES and IES. He has been serving all these societies in different capacities. He has received the IES 2009 Early Career Award, the IES 2011 Anthony J. Hornfeck Service Award, the 2014 Dr. Bimal Bose Energy Systems Award, the 2011 Industrial Electronics Magazine best paper award and the Third Prize paper award by the Industrial Power Converter Committee at ECCE 2012, 2012, 2017 IEEE PELS Sustainable Energy Systems Technical Achievement Award and the 2018 IEEE-IES Mittelman Achievement Award.



Frede Blaabjerg (S'86-M'88-SM'97-F'03) was with ABB-Scandia, Randers, Denmark, from 1987 to 1988. From 1988 to 1992, he got the PhD degree in Electrical Engineering at Aalborg University in 1995. He became an Assistant Professor in 1992, an Associate Professor in 1996, and a Full Professor of power electronics and drives in 1998. From 2017 he became a Villum Investigator. He is honoris causa at University Politehnica Timisoara (UPT), Romania and Tallinn Technical University (TTU) in Estonia.

His current research interests include power electronics and its applications such as in wind turbines, PV systems, reliability, harmonics and adjustable speed drives. He has published more than 600 journal papers in the fields of power electronics and its applications. He is the co-author of four monographs and editor of ten books in power electronics and its applications.

He has received 32 IEEE Prize Paper Awards, the IEEE PELS Distinguished Service Award in 2009, the EPE-PEMC Council Award in 2010, the IEEE William E. Newell Power Electronics Award 2014, the Villum Kann Rasmussen Research Award 2014, the Global Energy Prize in 2019 and the 2020 IEEE Edison Medal. He was the Editor-in-Chief of the IEEE TRANSACTIONS ON POWER ELECTRONICS from 2006 to 2012. He has been Distinguished Lecturer for the IEEE Power Electronics Society from 2005 to 2007 and for the IEEE Industry Applications Society from 2010 to 2011 as well as 2017 to 2018. In 2019-2020 he serves a President of IEEE Power Electronics Society. He is Vice-President of the Danish Academy of Technical Sciences too.

He is nominated in 2014-2019 by Thomson Reuters to be between the most 250 cited researchers in Engineering in the world.